



# Boron-doped porous carbon boosts electron transport efficiency for enhancing Fenton-like oxidation capacity: High-speed driving of Fe(III) reduction

Huanjing Zhang<sup>a,1</sup>, Cheng Chen<sup>b,\*1</sup>, Muke Lin<sup>a</sup>, Lingzhi Zhou<sup>a</sup>, Hailing Wen<sup>a</sup>, Tao Zhong<sup>a</sup>, Huinan Zhao<sup>a,c</sup>, Shuanghong Tian<sup>a,c</sup>, Chun He<sup>a,c,\*\*</sup>

<sup>a</sup> School of Environmental Science and Engineering, Sun Yat-sen University, Guangzhou 510006, China

<sup>b</sup> Department of Environmental Science and Engineering, University of Science and Technology of China, Hefei 230026, China

<sup>c</sup> Guangdong Provincial Key Laboratory of Environmental Pollution Control and Remediation Technology, Guangzhou 510006, China

## ARTICLE INFO

**Keywords:**  
Fe(III)/Fe(II) redox cycle  
Cocatalyst  
Boron doping  
Fe(III) reduction routes  
Fenton-like reaction

## ABSTRACT

Herein, Fenton-like cocatalysts with sufficient activity and stability were developed to accelerate the Fe(III)/Fe(II) redox cycle, thereby enhancing the oxidation capacity of Fe(III)/H<sub>2</sub>O<sub>2</sub> system. A porous engineering coupled with heteroatom doping strategy was adopted to prepare high-performance cocatalysts represented by boron-doped porous carbon (BPC). A small amount of BPC input (0.04 g/L) drives the efficient degradation of pollutants in Fe(III)/H<sub>2</sub>O<sub>2</sub> system via •OH-dominated radical pathway. Based on characterization results, the doping of boron species optimizes the pore structure of cocatalysts and improves their co-catalytic activity. Meanwhile, boron content increase steers the reduction of Fe(III) in BPC/Fe(III)/H<sub>2</sub>O<sub>2</sub> system through an “expressway” with higher electron transport efficiency. Theoretical calculations suggested the “electron porter” effect of BCO<sub>2</sub> on BPC to produce free Fe(II) for H<sub>2</sub>O<sub>2</sub> activation. The continuous-flow device using BPC as a membrane component has excellent performance in purifying micro-polluted water. This study provides a novel co-catalytic Fenton-like method for water remediation.

## 1. Introduction

Fenton process, with the merits of high efficiency and simple operation, is the most useful modern oxidation technique for water pollution control [1–3]. Under acidic circumstances, Fe(II) can react with hydrogen peroxide (H<sub>2</sub>O<sub>2</sub>) to generate hydroxyl radicals (•OH, E<sub>0</sub> = 2.80 V/NHE) (Eq. 1), which is a powerful weapon to degrade persistent contaminants and inactivate pathogens. [4–7]. However, the main obstacle in front of the development of Fenton process is the Fe species transition from Fe(III) to Fe(II) because of its sluggish kinetics (Eq. 2) [8, 9]. Due to untimely electronic replenishment, sustainable and efficient oxidation performance cannot be achieved.



To overcome this issue, the primary concern is to accelerate the reduction of Fe(III). In recent years, heterogeneous cocatalysts have attracted increasing attention due to their recyclability, structural adjustability and strong reducibility [10]. Xing et al. found that zero-valent metals (e.g., Mo<sup>0</sup> [11]) and metal sulfides/oxides (e.g., MoS<sub>2</sub> [12–15], WS<sub>2</sub> [16], and MoO<sub>3</sub> [17]) had good capacity to boost the Fe(III)/Fe(II) redox cycle. To avoid metal ion leaching, scholars have also developed a series of metal-free cocatalyst materials, such as multi-walled carbon nanotubes [18,19], crystalline boron [20] and black red phosphorus [21]. Carbon-based materials stand out from the aforementioned materials owing to better environmental friendliness [10], but their co-catalytic activity is still expected to be further improved.

Heteroatom doping tactics are the effectual measures to modify the co-catalytic characteristics of carbon materials [22,23], among which boron doping has definitely attracted scientists' attention in the design

\* Corresponding author.

\*\* Corresponding author at: School of Environmental Science and Engineering, Sun Yat-sen University, Guangzhou 510006, China.

E-mail addresses: [cc\\_env@mail.ustc.edu.cn](mailto:cc_env@mail.ustc.edu.cn) (C. Chen), [hechun@mail.sysu.edu.cn](mailto:hechun@mail.sysu.edu.cn) (C. He).

<sup>1</sup> Huanjing Zhang and Cheng Chen contributed equally to this work.

of metal-free catalysts [24–26]. Boron ( $\chi_B = 2.04$ ) has a lower electronegativity than carbon ( $\chi_C = 2.55$ ), exhibiting a lower Fermi level and a tendency to readily lose electrons [26]. The relatively small atomic radius of boron makes it easy to enter the carbon lattice and replace  $sp^2$  and  $sp^3$  structures, thus improving the electronic conductivity of carbon materials [27]. Density functional theory (DFT) calculations further demonstrate that boron doping can induce a polarization phenomenon on the carbon surface, promoting electrostatic and ion- $\pi$  interactions between the material surface and solution ions [28]. Considering these properties, boron-doped carbon materials hold promise as excellent co-catalysts to enhance the oxidation ability of Fenton-like systems. Although boron-containing materials (such as amorphous/crystalline boron and boron carbide [29]) have been reported to accelerate Fe(III) reduction, there is currently no research on the use of boron-doped carbon materials as Fenton-like cocatalysts.

For the co-catalytic Fe(III) reduction mechanism, the B-B bond on the surface of crystalline boron can directly provide electrons to Fe(III), releasing homogeneous Fe(II) for  $H_2O_2$  activation [20,30]. Different from the boron system, the interfacial electron transfer caused by the complexation of iron ions with cocatalysts is the key to the reduction of Fe(III) in carbon materials (such as carbon nanotubes [18], hydrophilic mesoporous carbon [31] and fullerol [32]) co-catalytic systems, and the activation of  $H_2O_2$  happens on the surface of carbon materials. Containing both B and C atoms, boron carbide ( $B_4C$ ) enhances the reduction of Fe(III) by  $H_2O_2$  by increasing the redox potential of Fe(III) [29]. Obviously, different co-catalytic principles are involved in different boron-based and carbon-based cocatalysts, which is worth considering whether the reduction pathway of Fe(III) in the corresponding systems can be regulated by adjusting the proportion of carbon and boron in the materials. Therefore, it is very meaningful to study the influence of boron doping on the co-catalytic mechanism modulation of carbonaceous cocatalysts.

Micro-morphological structure control is another approach to endow material with fascinating properties. Motivated by the observation that the self-assembly process amongst precursors might result in the creation of distinct three-dimensional porous morphologies via intense hydrogen bonding reactions [33], we explored the potential of combining porous engineering with boron doping to create innovative cocatalysts. Consequently, boron-doped porous carbon materials (BPC) with optimized carbon skeleton structure were synthesized by a one-step carbonization method based on the self-assembly reaction between boron-containing precursors [34–36]. The involvement of BPC pre-eminently elevated the oxidation capability of Fe(III)/ $H_2O_2$  system towards diverse organic contaminants. Combined with experimental and theoretical calculation results, the role of boron doping for tailoring co-catalytic activity and Fe(III) reduction pathway involved in BPC/Fe(III)/ $H_2O_2$  system was systematically evaluated, and the primary oxidation mechanism was identified. Finally, the successful attempt of BPC co-catalytic membrane in continuous flow experiments verified its feasibility in practical water treatment. This study constructed a novel BPC/Fe(III)/ $H_2O_2$  oxidation system and provided new insights into Fe(III) reduction mechanism modulation in heteroatom-doped carbon material assisted Fenton-like systems.

## 2. Experimental section

### 2.1. Preparation of BPC cocatalyst

A typical procedure for synthesizing BPC cocatalyst is listed as follows. First, a certain amount of glucose (0.01 mol), sodium bicarbonate (0.02 mol) and 30 mL of water were added into a 50 mL beaker and stirred in a 100 °C water bath. After the solid is completely dissolved, a certain proportion of boric acid (0 mmol, 10 mmol, 15 mmol, 20 mmol, 30 mmol) was added. About two hours later, the mixture was collected and transferred into a combustion boat. Then, the combustion boat was placed into a tube furnace with the protection of  $N_2$  atmosphere, which

was further pyrolyzed at 900 °C for 2.0 h to obtain BPC composites (heating rate: 5 °C/min). Subsequently, the sample after natural cooling was washed repeatedly with ethanol and deionized water via suction filtration. Finally, the target BPC cocatalyst was collected after drying in a vacuum oven. The prepared cocatalysts are referred to as PC, BPC-10, BPC-15, BPC-20, and BPC-30, respectively, depending on the molar amount of boric acid added to the precursor. The precursor of BPC-30 pyrolyzed at different temperatures (i.e., 600 °C, 700 °C, 800 °C and 900 °C) were denoted as BPC<sub>600</sub>, BPC<sub>700</sub>, BPC<sub>800</sub> and BPC<sub>900</sub>.

### 2.2. Experimental procedures

In this study, all experiments were conducted in a 100 mL beaker, stirred using a stirrer at 500 rpm to maintain homogeneity during the reaction. Typically, pollutants (e.g., caffeine (CAF), sulfamethoxazole (SMX), paracetamol (PCM), ibuprofen (IPB), naproxen (NPX), carbamazepine (CBZ) and nitrobenzol (NB), Table S1) are degraded by adding a certain amount of cocatalyst (for boosting the iron ion cycle), ferric nitrate solution (5.0 mM) and  $H_2O_2$  (30%) into 50 mL of pollutant solution (10.0 mg/L). If not stated otherwise, the temperature was controlled at 25 °C, and the pH of the solution had been adjusted to 4.0 in advance using nitric acid and sodium hydroxide. At specific time intervals during the reaction, 1.0 mL of the sample was withdrawn and filtered using a 0.22 μm film. Then, the reaction was quenched by adding 0.5 mL of methanol. Assays of organic compounds in samples were conducted using high-performance liquid chromatography (HPLC, Shimadzu Essentia LC-16, Japan) with a C18 column (WondaSil C18-WR 5 m, 4.6 × 15 cm), detailed test conditions are provided in Table S2.

### 2.3. Characterizations and analytical methods

Elemental composition and chemical valence state information of different cocatalysts were obtained by X-ray photoelectron spectroscopy (XPS) of Thermo Scientific K-alpha under Al K $\alpha$  radiation ( $h\nu = 1486.6$  eV). Raman spectra of samples were obtained using a miniature Raman spectrometer (Renishaw inVia, UK) equipped with laser excitation at 633 nm. The specific surface area, pore volume and pore distribution of the samples were determined by physical adsorption of  $N_2$  at 77 K on an auto-adsorption system (Auto Chem II 2920, Micromeritics, Inc., USA). The morphology of the prepared materials was observed by field emission scanning electron microscopy (FESEM, FEI Quanta 400 F, the Netherlands). The crystal structure of cocatalysts was analyzed by an X-ray diffractometer equipped with Cu K $\alpha$  radiation (Rigaku UltimaIV, Japan). The Fourier transform infrared spectrometer (FTIR, Bruker EQUINOX 55) was used to gain the functional group information of cocatalysts. The concentrations of free ferrous ions and total free iron species were detected by the 1,10-phenanthroline method using a 752 G UV-visible spectrophotometer (INESA 752 G, Shanghai) [37]. Modified ammonium metavanadate spectrophotometric method was used to measure the  $H_2O_2$  concentration in the solution [38]. Electrochemical analysis was performed on an electrochemical workstation (CHI 660E, CH Instrument, China) with a three-electrode cell system. More experimental details are presented in the Supporting Information.

## 3. Results and discussion

### 3.1. Morphology and co-catalytic oxidation behaviors of BPC

As shown in Figs. 1a-b, the overall morphology of the BPC-30 material reflected a rough, micron-sized chip with densely spaced holes on the surface. The staggered three-dimensional (3D) internal channels might be attributed to the strong hydrogen-bonding interactions between boric acid, sodium bicarbonate and water molecules, which triggered the self-assembly reaction and formed the pore-crosslinked stereo structure during the carbonization of precursors [34–36]. Additionally, the elements mapping analysis (Figs. 1c-f) showed that boron

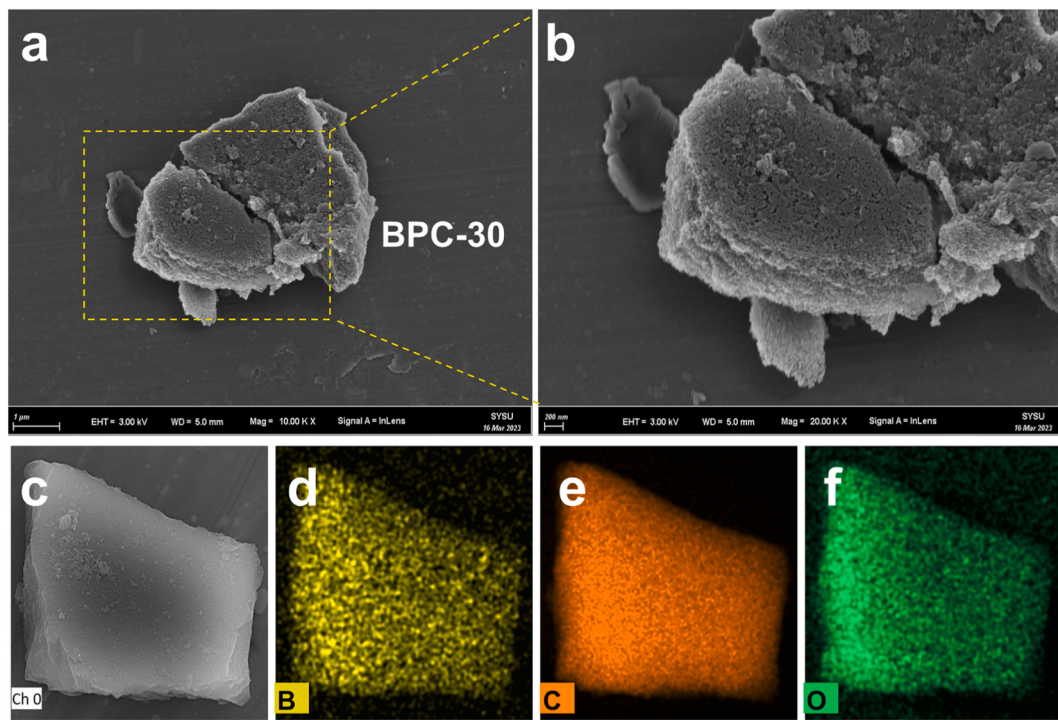


**Fig. 1.** SEM images of BPC-30: Mag = 10.00 K X (a), Mag = 20.00 K X (b); Element mapping images of BPC-30: sample (c), B (d), C (e) and O (f).

atoms are evenly distributed on BPC-30. The aforementioned findings indicated that the boron-doped porous carbon material was successfully synthesized.

To assess the efficacy of BPC cocatalyst in improving the oxidation performance of Fe(III)/H<sub>2</sub>O<sub>2</sub> system, degradation experiments were carried out selecting caffeine (CAF) as the model pollutant. As shown in Fig. 2a, sole BPC could not effectively activate H<sub>2</sub>O<sub>2</sub> and only ~10% of CAF was adsorbed by BPC. Likewise, Fe(III)/H<sub>2</sub>O<sub>2</sub> system had essentially little impact on the degradation of CAF at pH 4.0. Of note, after adding BPC (0.04 g/L), CAF was completely degraded within 30 min at a reaction constant rate ( $k_{obs}$ ) of  $(1.30 \pm 0.20) \times 10^{-1} \text{ min}^{-1}$  (Fig. 2a). The great improvement in CAF removal indicated that BPC manifests a remarkable co-catalytic capacity to boost the cycle of Fenton-like reaction for the oxidation of pollutants. The effects of BPC, Fe(III) and H<sub>2</sub>O<sub>2</sub> concentrations on CAF elimination were then analyzed under diverse experimental settings. It was evident that the CAF degradation rate increased to varying degrees as the concentration rose (Figs. 2b-d). By modelling experimental data using the pseudo-first-order kinetics model (Figure S1), the total rate equation of CAF degradation in BPC/Fe(III)/H<sub>2</sub>O<sub>2</sub> system was obtained, displayed as Eq. 3. The more significant reaction order of H<sub>2</sub>O<sub>2</sub> concentration suggested that it had a rather considerable impact on the ability to degrade CAF.

$$v = -\frac{dc}{dt} = 3.6060 \times 10^{-2} [\text{BPC}]_0^{0.3666} [\text{Fe(III)}]_0^{0.5492} [\text{H}_2\text{O}_2]_0^{0.6341} \quad (3)$$

Next, the influence of pH (3.0–7.0) on the oxidation capacity of BPC/Fe(III)/H<sub>2</sub>O<sub>2</sub> system was investigated. As displayed in Figure S2, the zeta potential of BPC decreases with increasing pH and the isoelectric point is between pH 1.2 and 2.0, implying BPC is negatively charged in the pH range of 3.0–7.0. Fig. 2e showed BPC/Fe(III)/H<sub>2</sub>O<sub>2</sub> system maintained a high level of oxidation activity at acidic conditions (i.e., pH 3.0 and 4.0), which was able to completely degrade CAF in 60 min. Interestingly, pH 4.0 provided the best performance, consistent with previous studies [9, 23]. It can be explained by the fact that an appropriately raised pH facilitates the interaction between positively charged Fe(III) species and BPC owing to the enhanced electrostatic attraction. With the weakening of the acidity, only ~50% of CAF was eliminated after 60 min at pH 5.0,

and BPC/Fe(III)/H<sub>2</sub>O<sub>2</sub> system had negligible oxidation capacity under neutral circumstances due to the hydrolytic inactivation of Fe(III) species.

The general applicability, anti-interference ability and stability of BPC/Fe(III)/H<sub>2</sub>O<sub>2</sub> system were further focused. Fig. 2f demonstrated that a wide array of pollutants (e.g., CAF, NPX, CBZ, SMX, PCM and IBP) could be effectively removed within 30 min, indicating BPC/Fe(III)/H<sub>2</sub>O<sub>2</sub> system exhibited excellent non-selective oxidation capabilities for diverse contaminants removal. Fig. 2g illustrates the effect of coexisting anions and humic acids on the elimination of CAF in BPC/Fe(III)/H<sub>2</sub>O<sub>2</sub> system. The oxidation efficiency was marginally decreased by the addition of chloride (Cl<sup>-</sup>), bicarbonate (HCO<sub>3</sub><sup>-</sup>) and humic acid, which could be attributed to the formation of reactive species with low redox potential or the competitive consumption of reactive oxygen species (ROS) during reactions [39]. However, CAF degradation was significantly inhibited in the presence of dihydrogen phosphate (H<sub>2</sub>PO<sub>4</sub><sup>-</sup>), which was attributed to that H<sub>2</sub>PO<sub>4</sub><sup>-</sup> captured Fe(III) ions to result in the ineffective activation of H<sub>2</sub>O<sub>2</sub> [40]. CAF decomposition by BPC/Fe(III)/H<sub>2</sub>O<sub>2</sub> system in different water matrices (including tap water, surface water and WWTP effluent from the secondary sedimentation tank, the corresponding water quality parameters are listed in Table S3) was further examined. The removal rate of CAF only showed a small decrease and it can still reach more than 90% after 60 min in all types of waters (Fig. 2h), which illustrates the viability of using BPC/Fe(III)/H<sub>2</sub>O<sub>2</sub> system for actual water treatment. Cyclic tests were used to evaluate the reusability of the BPC cocatalyst. As shown in Fig. 2i, most of CAF (~90%) could still be removed after a 4-hour cycle, demonstrating its long-term co-catalytic activity.

### 3.2. Effect of boron doping on the optimized cocatalyst structure and activity

Initially, XPS was used to examine the element composition of as-prepared PC and BPC with different boron doping amounts (i.e., BPC-10, BPC-15, BPC-20 and BPC-30). As shown in Figure S5, the boron content in the cocatalyst increased accordingly with the increase of boric acid dosage in the preparation process. Four peaks were observed in the

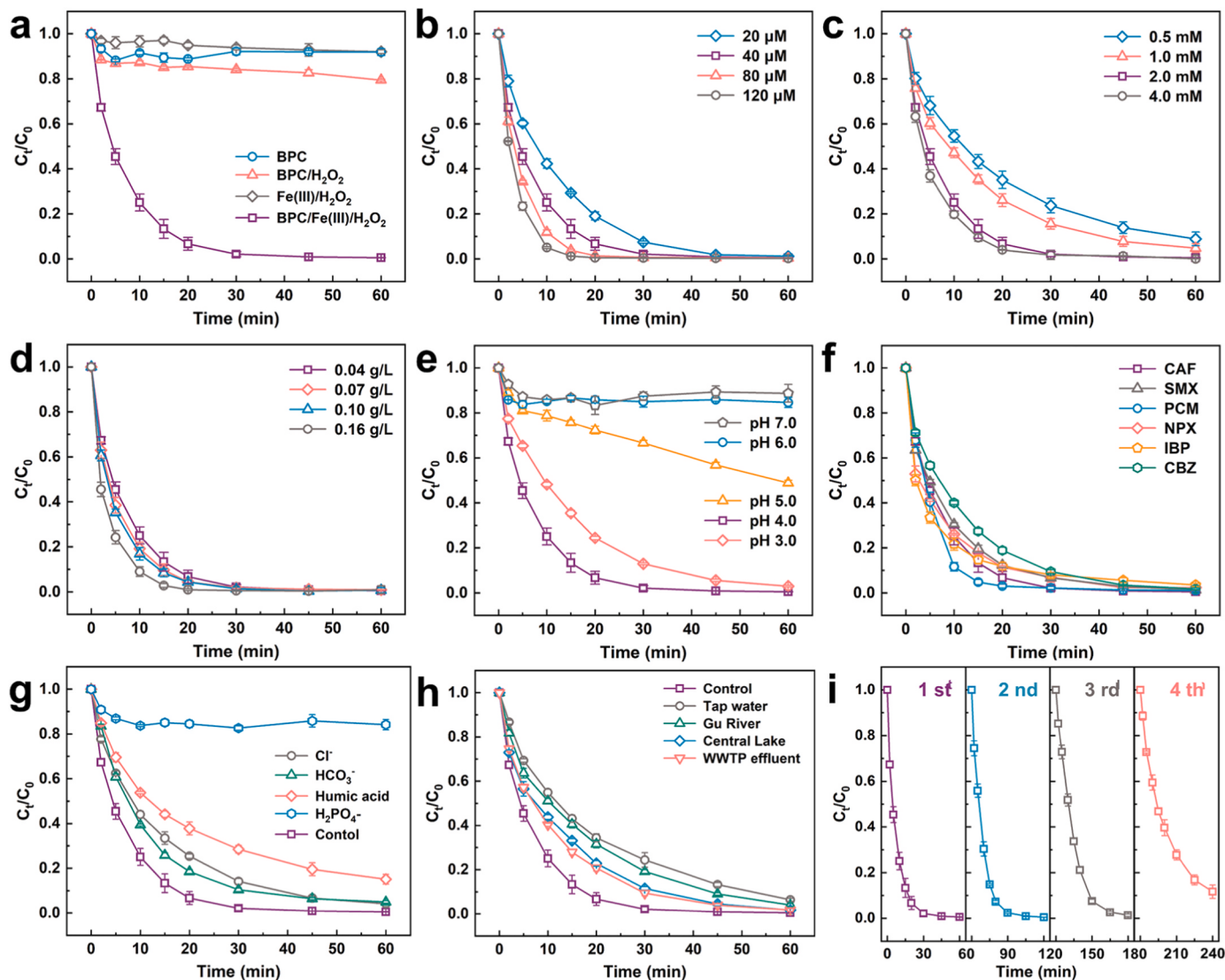


**Fig. 2.** (a) CAF removal by sole BPC, BPC/H<sub>2</sub>O<sub>2</sub>, Fe(III)/H<sub>2</sub>O<sub>2</sub> and BPC/Fe(III)/H<sub>2</sub>O<sub>2</sub> systems; Effects of Fe(III) concentration (b), H<sub>2</sub>O<sub>2</sub> concentration (c) and BPC dosage (d) on CAF degradation in BPC/Fe(III)/H<sub>2</sub>O<sub>2</sub> system; (e) CAF degradation in BPC/Fe(III)/H<sub>2</sub>O<sub>2</sub> systems under different pH conditions; (f) Different pollutants degradation in BPC/Fe(III)/H<sub>2</sub>O<sub>2</sub> system; (g) CAF degradation in BPC/Fe(III)/H<sub>2</sub>O<sub>2</sub> system with the coexisting of anions and humic acid; (h) CAF degradation in various actual water matrices by BPC/Fe(III)/H<sub>2</sub>O<sub>2</sub> system; (g) Cycle test of CAF degradation in BPC/Fe(III)/H<sub>2</sub>O<sub>2</sub> system. If not specified otherwise, the BPC cocatalyst used in the experiments was BPC-30, [BPC-30]<sub>0</sub> = 0.04 g/L, [Fe(III)]<sub>0</sub> = 40.0 μM, [H<sub>2</sub>O<sub>2</sub>]<sub>0</sub> = 2.0 mM, [CAF]<sub>0</sub> = 10.0 mg/L, pH 4.0 and T = 25 °C.

B 1 s XPS spectra of BPC materials (Fig. 3a), which were assigned to BC<sub>3</sub> (~190.10 eV), BC<sub>2</sub>O (~191.34 eV), BCO<sub>2</sub> (~192.20 eV) and B-O (~193.44 eV), respectively [41]. Table S4 exhibited that boron in BPC mainly existed in the form of B-C-O species (including BC<sub>2</sub>O and BCO<sub>2</sub>), which was attributed to the doping of boron atoms caused the rearrangement of π electrons in the carbon plane, leading to the weakening of C-C bonds and the strengthening of C-O bonds in the process of electrophilic oxygen adsorption, thus forming more BC<sub>2</sub>O and BCO<sub>2</sub> functional groups [42,43].

Raman spectroscopy was used to investigate the effect of boron doping on the carbon structure of these cocatalysts. As shown in Fig. 3b, Raman spectra of PC and all BPC materials featured two distinct characteristic peaks at ~1360 cm<sup>-1</sup> and ~1590 cm<sup>-1</sup>, which correspond to the D band representing the in-plane defect energy level and the G band of sp<sup>2</sup>-hybrid carbon E<sub>2g</sub> vibration, respectively [44–46]. Therefore, the I<sub>D</sub>/I<sub>G</sub> value is able to reflect the graphitization or defect degree of the material [47]. With the increase of boron doping content in the cocatalyst (from PC to BPC-30), the I<sub>D</sub>/I<sub>G</sub> value gradually decreased from 1.11 to 0.87, indicating that the enrichment of boron content in favor of

enhancing the graphitization degree of porous carbon materials, thereby improving their electrical conductivity [48,49].

N<sub>2</sub> adsorption-desorption tests were conducted to examine the effects of boron doping on the surface characteristics and inner pore structure of as-prepared cocatalysts. Hysteresis loops appear in the relative pressure range of 0.45–0.98 in the adsorption-desorption isotherms of PC and different BPC materials (Figure S7), demonstrating that the pores in these materials are primarily mesoporous structures [50]. Once boron species were introduced, the BET specific surface area and pore volume of porous carbon materials were significantly increased (Table S6). This improvement was possibly caused by self-assembly reactions in BPC precursors, which made the materials create a three-dimensional structure with a larger specific surface area [51,52]. According to Figure S8, the most probable pore size of BPC-30 is 16.2918 nm, which is larger than the 3.9959 nm of PC. Therefore, boron doping leads to the creation of larger pore volume mesopores in materials, which increases their specific surface area and exposes additional catalytic reaction sites.

The performance of PC and different BPC materials as cocatalysts in

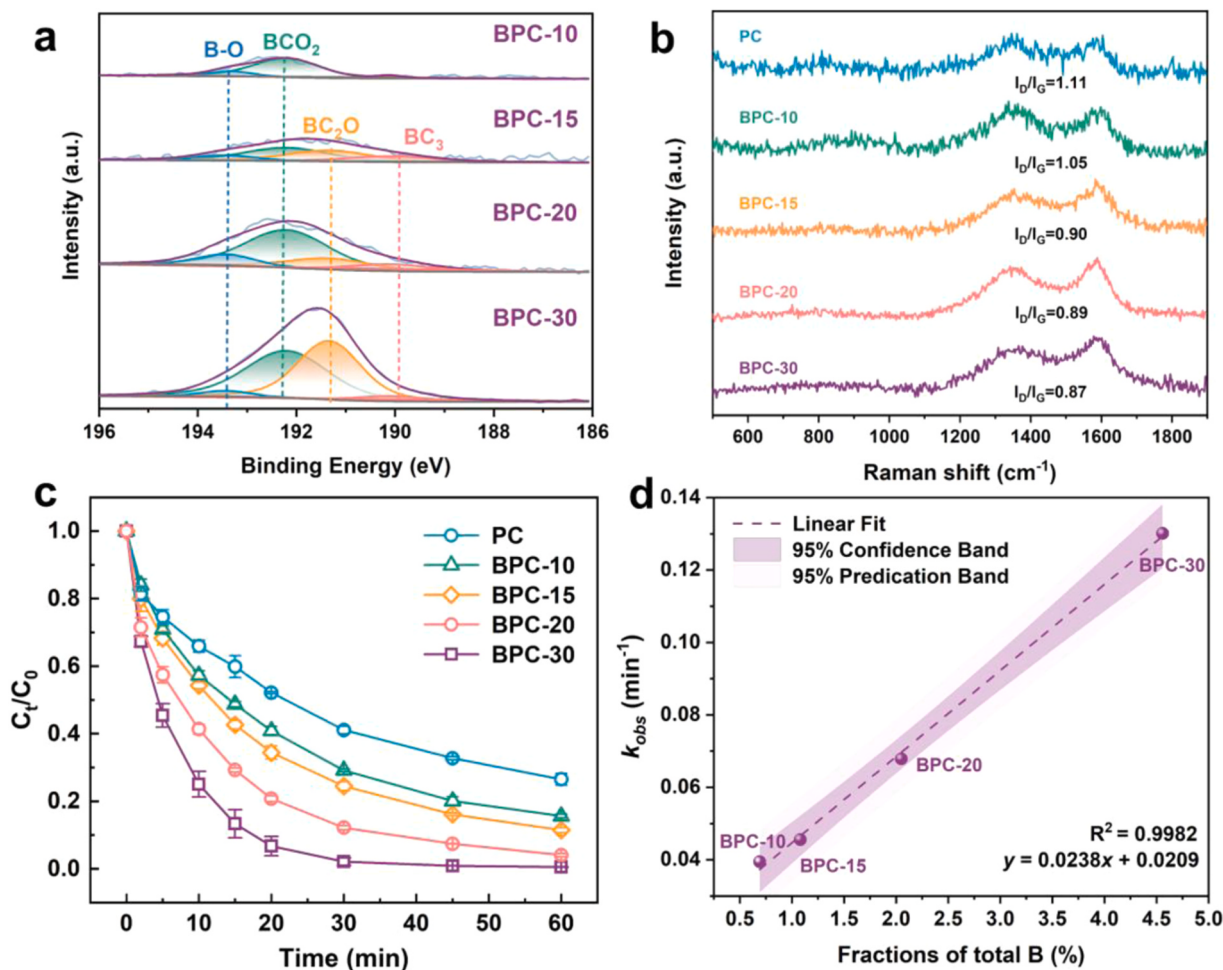


**Fig. 3.** (a) XPS B 1 s spectra of different BPC cocatalysts; (b) Raman spectra of PC and different BPC cocatalysts; (c) CAF removal by PC/Fe(III)/H<sub>2</sub>O<sub>2</sub> and different BPC/Fe(III)/H<sub>2</sub>O<sub>2</sub> systems; (d) Correlation between total B content in BPC and  $k_{obs}$  of CAF degradation in different BPC/Fe(III)/H<sub>2</sub>O<sub>2</sub> systems ( $[BPC]_0 = 0.04$  g/L, [Fe(III)]<sub>0</sub> = 40.0  $\mu$ M, [H<sub>2</sub>O<sub>2</sub>]<sub>0</sub> = 2.0 mM, [CAF]<sub>0</sub> = 10.0 mg/L, pH 4.0, T = 25 °C).

Fe(III)/H<sub>2</sub>O<sub>2</sub> system was evaluated (Fig. 3c). The  $k_{obs}$  of CAF degradation in different BPC/Fe(III)/H<sub>2</sub>O<sub>2</sub> systems rose from  $(3.94 \pm 0.03) \times 10^{-2} \text{ min}^{-1}$  (BPC-10 co-catalytic system) to  $(1.30 \pm 0.22) \times 10^{-1} \text{ min}^{-1}$  (BPC-30 co-catalytic system), which is linearly dependent on the amount of boron in BPC ( $R^2 = 0.9982$ ). A similar fine linear correlation between  $k_{obs}$  and boron content in the cocatalyst ( $R^2 = 0.9920$ ) was also obtained by using BPC prepared at different pyrolysis temperatures to enhance CAF oxidation in Fe(III)/H<sub>2</sub>O<sub>2</sub> system (Figure S9). Therefore, the fact that boron doping can significantly enhance the reactivity of BPC to boost Fenton-like oxidation was demonstrated.

Taken together, boron doping has achieved appreciable effects on improving pore structure in BPC materials, which also enhances the graphitization degree and provides more reaction sites for co-catalytic reactions, leading to better performance in degrading pollutants.

### 3.3. Intensified Fe(III) reduction and related route analysis

Previous studies have demonstrated that there are primarily three approaches for reducing Fe(III) in a co-catalyzed Fenton-like oxidation system: (i) Cocatalyst as a reducing agent [53] or electron sacrificial agent [20,30,54] to directly reduce Fe(III), in this way, iron species mainly existed in the dissolved state; (ii) Fe(III) reacting with the cocatalyst to form a complex, then be reduced via interfacial electron transfer (the cocatalyst acts as an electron shuttle, transferring electrons from the donor to Fe(III)) [18,23,31,32], and in this case, iron species mainly exist in the surface-bound state; (iii) Enhancing the reactivity

between Fe(III) and H<sub>2</sub>O<sub>2</sub> by raising the redox potential of Fe(III), thus facilitating the reduction of Fe(III) by H<sub>2</sub>O<sub>2</sub> [22,29].

Iron species analysis was carried out to uncover Fe(III) reduction pathways in BPC/Fe(III)/H<sub>2</sub>O<sub>2</sub> systems. As the reaction progressed, a portion of Fe(III) was converted to Fe(II) and the detected Fe(II) concentration at 5.0 min in different systems ranged from 6.54  $\mu$ M (PC/Fe(III)/H<sub>2</sub>O<sub>2</sub>) to 7.71  $\mu$ M (BPC-30/Fe(III)/H<sub>2</sub>O<sub>2</sub>) (Fig. 4a). Then, the free Fe(II) gradually decreased with time, which was attributed to part of iron species being bound on the BPC surface. The characteristic peak of Fe(II) in XPS Fe 2p spectra of reacted BPC-30 (Fig. 4b) obviously revealed the reactivity of BPC-30 for direct reduction of Fe(III), which demonstrated that the Fe(III)/Fe(II) transition happened on the surface of BPC-30. To further discern the differences in the Fe(III) reduction capacity of BPC materials, variations of free iron in PC/Fe(III) and different BPC/Fe(III) systems were investigated. As shown in Fig. 4c, the reduction performance of BPC for Fe(III) is undoubtedly superior to that of PC, and the reduction capacity increases as the boron level in BPC materials rises (from BPC-10 to BPC-30).

Electrochemical analysis was performed to explore the origin of boron doping for enhancing the capacity of cocatalysts to reduce Fe(III). Initially, the potential redox reactions of PC and different BPC materials in Fe(III) solution were evaluated by cyclic voltammetry (CV). As indicated by Figs. 4d and S10, the CV curves of all materials had patent cathode peaks and anode peaks, proving that the Fe(III)/Fe(II) cycle was present on the cocatalyst during scanning. The peak-to-peak separation ( $\Delta E_p$ , the potential difference between the cathode peak and anode

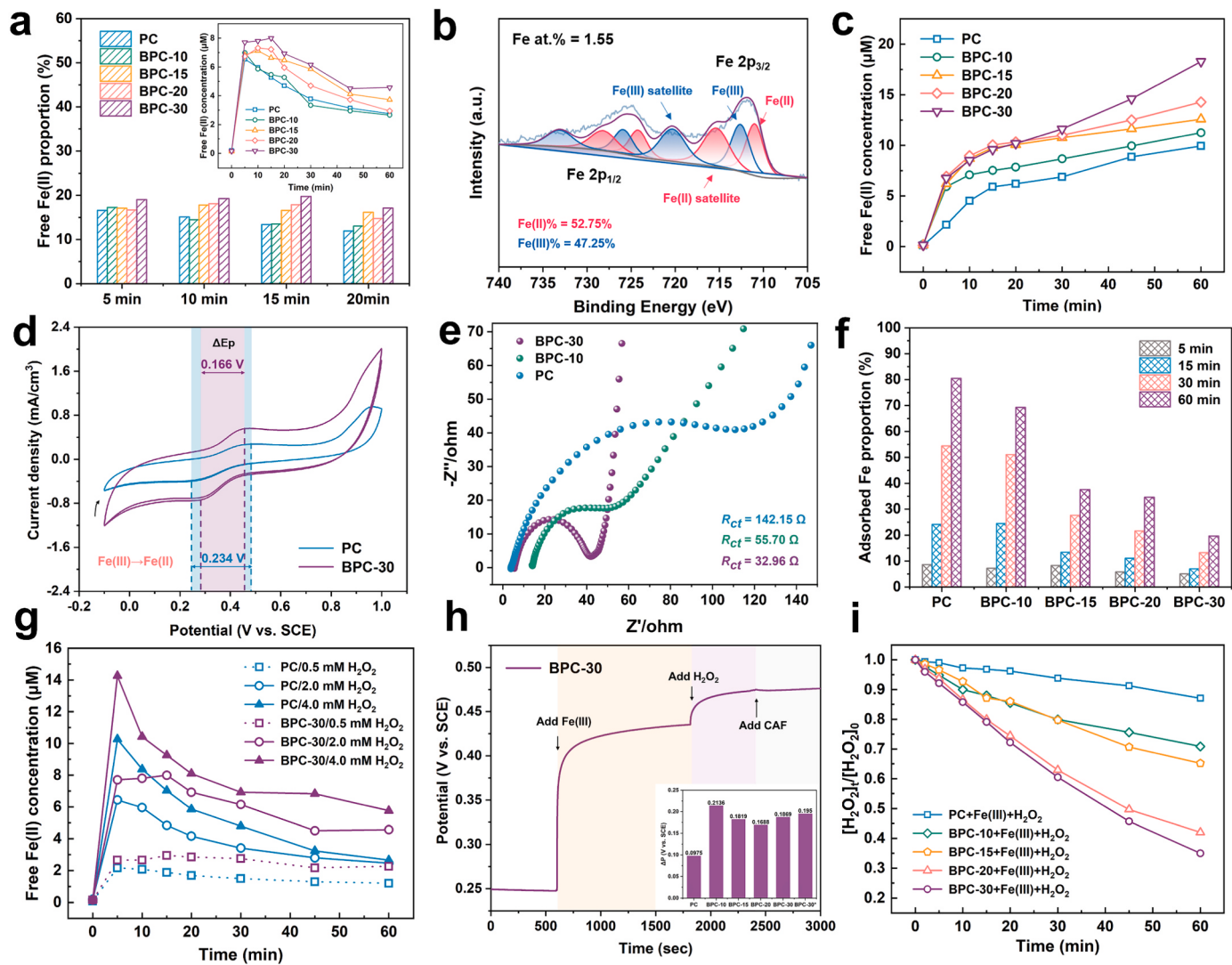


**Fig. 4.** (a) Variations of free Fe(II) proportion and time profiles of free Fe(II) concentration (inset) in PC/Fe(III)/ $\text{H}_2\text{O}_2$  and different BPC/Fe(III)/ $\text{H}_2\text{O}_2$  systems; (b) XPS Fe 2p spectra of used BPC-30; (c) Time profiles of free Fe(II) concentration in PC/Fe(III) and different BPC/Fe(III) systems; (d) CV curves on PC and BPC-30 electrodes in Fe(III) solution ( $[\text{Fe(III)}]_0 = 5.0 \text{ mM}$ ,  $[\text{Na}_2\text{SO}_4]_0 = 0.5 \text{ M}$ , scan rate:  $10 \text{ mV/s}$ ); (e) Nyquist plots of PC, BPC-10 and BPC-30; (f) Adsorbed Fe proportions with time in PC/Fe(III)/ $\text{H}_2\text{O}_2$  and different BPC/Fe(III)/ $\text{H}_2\text{O}_2$  systems; (g) Time profiles of free Fe(II) concentration in PC/Fe(III)/ $\text{H}_2\text{O}_2$  and BPC-30/Fe(III)/ $\text{H}_2\text{O}_2$  systems at different  $\text{H}_2\text{O}_2$  concentrations; (h) Open-circuit potential curves on BPC-30 electrode after adding different substances, inset: the elevated potentials on different electrodes after adding Fe(III); (i) Time profiles of  $\text{H}_2\text{O}_2$  concentration in PC/Fe(III)/ $\text{H}_2\text{O}_2$  and different BPC/Fe(III)/ $\text{H}_2\text{O}_2$  systems ( $[\text{PC or BPC}]_0 = 0.04 \text{ g/L}$ ,  $[\text{Fe(III)}]_0 = 40.0 \mu\text{M}$ ,  $[\text{H}_2\text{O}_2]_0 = 2.0 \text{ mM}$ , pH 4.0, T = 25 °C).

peak) can indicate the reversibility of electrode reaction and is typically used to evaluate the difficulty of converting Fe(III) into Fe(II) on different cocatalysts [23,29]. Compared with PC ( $\Delta E_p = 0.234 \text{ V}$ ), the  $\Delta E_p$  of BPC electrodes decreased significantly. Moreover, it showed a trend toward decline with an increase in boron content, among which the  $\Delta E_p$  for BPC-30 was only  $0.166 \text{ V}$  (Fig. 4d). The results indicated that boron doping reduces the reaction energy barrier of Fe(III) to Fe(II), which facilitates the reduction of Fe(III) by BPC. Electrochemical impedance spectroscopy (EIS) testing was further used to evaluate the electron transport properties of BPC materials. The semicircular diameter of the Nyquist curve represented the charge transfer resistance ( $R_{ct}$ ) at the electrode-electrolyte solution interface [55,56]. As shown in Fig. 4e, the calculated  $R_{ct}$  of PC, BPC-10 and BPC-30 are  $142.15 \Omega$ ,  $55.70 \Omega$  and  $32.96 \Omega$ , respectively, indicating that the increase of boron content is conducive to improving the electron conductivity of the cocatalyst. To sum up, boron doping reduces the reaction barrier for the interconversion of Fe(III) and Fe(II) on the cocatalyst, and the increase of boron content further improves the conductivity of the material,

thereby enhancing the direct reduction ability of BPC to Fe(III).

Fig. 4f displayed that the majority of iron species existed in the adsorbed state in PC and BPC-10 co-catalytic systems after a 60-min reaction, whose fraction reached 80.46% and 69.24% respectively. With increasing boron content in BPC, the fraction of free iron species rose steadily, and 80.34% of iron species were dissolved in BPC-30/Fe(III)/ $\text{H}_2\text{O}_2$  system (Figure S11). The reduction pathway of Fe(III) in co-catalytic systems was related to the existence form of iron species. Considering the Fenton-like oxidation performance of different systems (Fig. 3c) and the distribution of iron species (Fig. 4f), it could be concluded that the cocatalyst-mediated interfacial electron transfer was not the main pathway for the Fe(III) reduction in BPC-30/Fe(III)/ $\text{H}_2\text{O}_2$  system, and Fe(III) in this system was more likely to be reduced by direct reaction with BPC-30 or  $\text{H}_2\text{O}_2$ . Therefore, the enrichment of boron content in the cocatalyst induces the transition of Fe(III) reduction from the interfacial electron transfer pathway to the cocatalyst direct reduction or  $\text{H}_2\text{O}_2$  reduction pathways.

Except for direct reduction by cocatalyst and reduction by cocatalyst-

mediated interfacial electron transfer, Fe(III) can also take electrons from H<sub>2</sub>O<sub>2</sub> in the system to effect reduction (Eq. 2). However, because of its sluggish kinetics, this approach strongly limits the sustainable generation of hydroxyl radicals. Hence, some studies focus on enhancing the redox potential of iron species to accelerate the reduction of Fe(III) by H<sub>2</sub>O<sub>2</sub> [22,29]. To investigate possible approaches for Fe(III) reduction by H<sub>2</sub>O<sub>2</sub> in PC and BPC co-catalytic systems, the free Fe(II) concentration in the systems with various H<sub>2</sub>O<sub>2</sub> concentrations was monitored. It can be seen in Fig. 4g, more free Fe(II) was detected in both PC and BPC-30 mediated systems as the H<sub>2</sub>O<sub>2</sub> concentration rose (Fig. 4g), demonstrating that H<sub>2</sub>O<sub>2</sub> participated in the reduction process of Fe(III). Comparing the differences of free Fe(II) concentration in PC/Fe(III)/H<sub>2</sub>O<sub>2</sub> and BPC-30/Fe(III)/H<sub>2</sub>O<sub>2</sub> systems at varying H<sub>2</sub>O<sub>2</sub> concentrations, more enhancement was observed in BPC-30 mediated system when the H<sub>2</sub>O<sub>2</sub> concentration was increased (Figure S12), which meant that the introduction of boron species further fostered the reaction of Fe(III) and H<sub>2</sub>O<sub>2</sub> to give more free Fe(II). Results from the open-circuit potential test also supported this finding. As shown in Fig. 4h, the open-circuit potential on the BPC-30 electrode significantly increased after the addition of Fe(III) at 600 s, reaching 0.1869 V at 1800 s. The potential increase following the addition of Fe(III) in BPC electrode system was significantly higher than that in PC electrode system (inset of Fig. 4h), indicating that boron doping increased the reactivity of the cocatalyst for Fe(III), further enhancing the Fe(III) reduction pathway where H<sub>2</sub>O<sub>2</sub> as the electron donor. Moreover, the H<sub>2</sub>O<sub>2</sub> consumption in different BPC co-catalytic systems increased with the increase of boron content in BPC and was greater than that in PC co-catalytic system (Fig. 4i), indicating that boron in the cocatalyst promoted the effective

utilization of H<sub>2</sub>O<sub>2</sub> in Fenton-like system (reducing Fe(III) or oxidizing pollutants after activation), which was consistent with the previous results of Fe(III) reduction and pollutant removal performance.

### 3.4. Comparison of different heteroatom-doped cocatalyst

Other porous carbon materials (i.e., NPC-30, SPC-30 and PPC-30) were also synthesized to investigate the effect of heteroatom doping on the regulation of co-catalytic activity and Fe(III) reduction routes in the corresponding systems. As shown in Fig. 5a, the doping of heteroatom did make an effect (compared with PC/Fe(III)/H<sub>2</sub>O<sub>2</sub> system in Fig. 3c), all these materials co-catalyzed Fe(III)/H<sub>2</sub>O<sub>2</sub> system could degrade pollutants effectively. The reduction mechanism of Fe(III) was then scrutinized. Fig. 5b shows all four materials exhibited the direct reduction capability to generate free Fe(II), among which BPC-30 manifested the best performance. Interestingly, more than 50% of iron species were adsorbed within 5.0 min in PPC-30 co-catalytic systems (Figs. 5c and S13), illustrating the electron-rich phosphorus site of PPC-30 promotes the surface binding of Fe(III) via electrostatic attraction [57]. The high ratio of adsorbed iron species also demonstrated that the cocatalyst-mediated interfacial electron transfer prevails for Fe(III) reduction. However, the electron transport efficiency seems unsatisfactory, causing the insufficient utilization of H<sub>2</sub>O<sub>2</sub> (Fig. 5d). SPC-30 and NPC-30 co-catalytic systems shared a similar variation trend of adsorbed iron species but differed in H<sub>2</sub>O<sub>2</sub> consumption (Fig. 5b-d), which was due to the different proportions of various Fe(III) reduction pathways. It was documented that N doping increases the reactivity of Fe(III) reduction by H<sub>2</sub>O<sub>2</sub>, and H<sub>2</sub>O<sub>2</sub> helps the interaction of Fe(III) species with

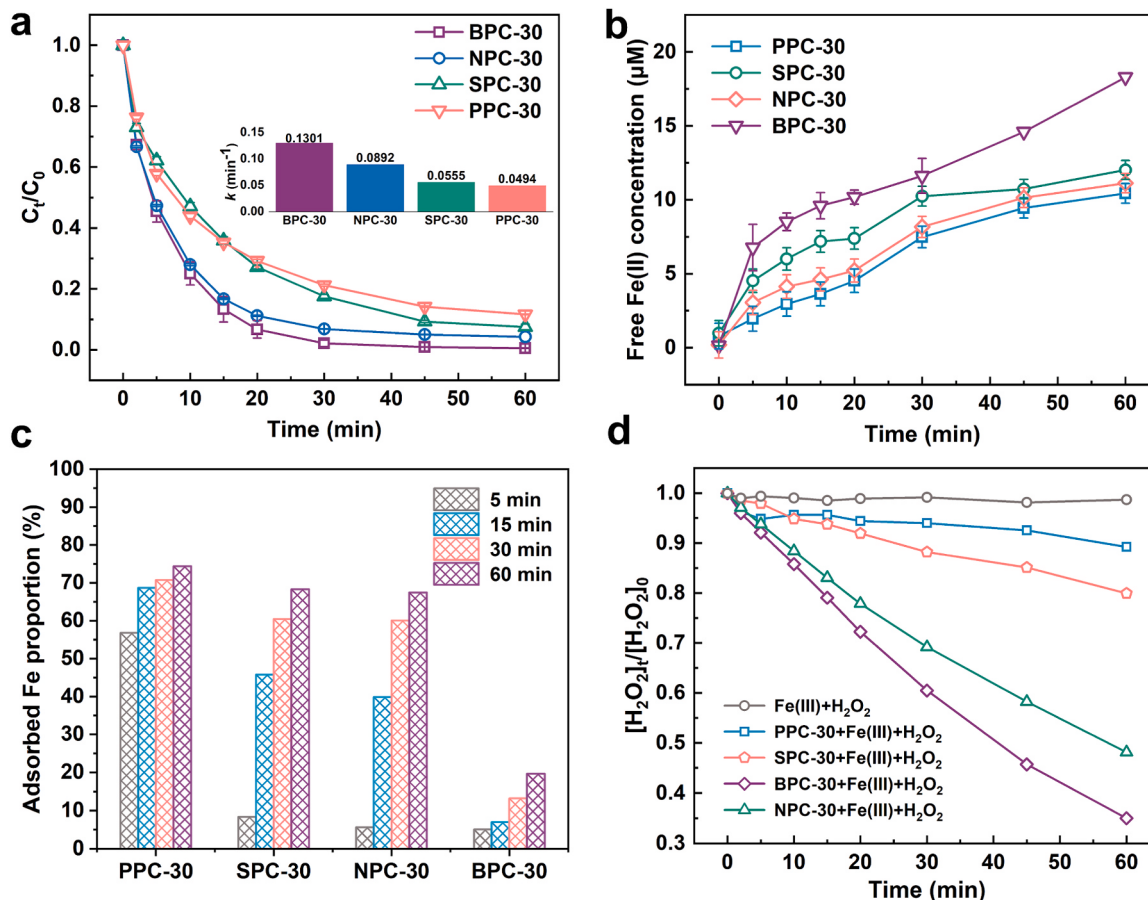


**Fig. 5.** (a) CAF removal and  $k_{obs}$  of CAF degradation by BPC-30, NPC-30, SPC-30 and PPC-30 co-catalyzed Fe(III)/H<sub>2</sub>O<sub>2</sub> systems; (b) Time profiles of free Fe(II) concentration in Fe(III) solutions reduced by BPC-30, NPC-30, SPC-30 and PPC-30; (c) Adsorbed Fe proportions with time in BPC-30, NPC-30, SPC-30 and PPC-30 co-catalyzed Fe(III)/H<sub>2</sub>O<sub>2</sub> systems; (d) Variations of H<sub>2</sub>O<sub>2</sub> concentration in Fe(III)/H<sub>2</sub>O<sub>2</sub> and BPC-30, NPC-30, SPC-30 and PPC-30 co-catalyzed Fe(III)/H<sub>2</sub>O<sub>2</sub> systems. If not specified otherwise, [cocatalyst]<sub>0</sub> = 0.04 g/L, [Fe(III)]<sub>0</sub> = 40.0  $\mu\text{M}$ , [H<sub>2</sub>O<sub>2</sub>]<sub>0</sub> = 2.0 mM, pH 4.0, T = 25 °C.

the N-doped cocatalyst to induce interfacial electron transfer [23]. Evidently, the doping of boron in boosting the co-catalytic oxidation performance of Fe(III)/H<sub>2</sub>O<sub>2</sub> system notably outperforms other dopants (Fig. 5a), which was credited to the switch in the conversion route and existence form of iron species enhanced the effective activation of H<sub>2</sub>O<sub>2</sub> by improving the mass transfer process (Fig. 5d). To sum up, heteroatom doping steers the co-catalytic properties of porous carbon materials and breeds distinctive Fe(III) reduction routes. Bearing the robust Fe(III) reduction efficiency, B-doped cocatalysts possess greater development potential.

### 3.5. DFT calculations and distinguish of active boron species

DFT calculations were performed to emulate the charge transfer between different boron species (B-O, BC<sub>2</sub>O, BCO<sub>2</sub>, BC<sub>3</sub>) and Fe(OH)<sub>2</sub><sup>+</sup> (the prime Fe(III) species at pH 4.0, 64.04%, Figure S15) on the molecular scale, and the corresponding interaction configurations were displayed in Figs. 6a and S16.

Firstly, the differential charge distribution diagram provided a clear visualization of the electron accumulation and loss distribution across Fe(OH)<sub>2</sub><sup>+</sup> on different BPC configurations (Fig. 6b), which was then quantitatively assessed by the Bader charge. In comparison to other models, Fe(III) accumulated more electrons (1.919 e) from BCO<sub>2</sub> configuration (Figs. 6c and S17), alluding to BCO<sub>2</sub> species on BPC may be more reactive for Fe(III) reduction. Similarly, the total electron loss of all C atoms and charge depletion in the B atom on the BCO<sub>2</sub> model run ahead among all configurations (Figs. 6d and S17), implying that the B and C atoms within this model were more likely to relinquish electrons, thereby reducing more Fe(III).

Next, the projected density of states (PDOS) was analyzed to further determine the main role of BCO<sub>2</sub> species. The d-band centers of Fe 3d orbitals in BCO<sub>2</sub> + Fe(OH)<sub>2</sub><sup>+</sup>, BC<sub>2</sub>O + Fe(OH)<sub>2</sub><sup>+</sup>, B-O + Fe(OH)<sub>2</sub><sup>+</sup>, and BC<sub>3</sub> + Fe(OH)<sub>2</sub><sup>+</sup> models are located at -0.8801, -0.9087, -1.0261 and -1.0418 eV, respectively (Fig. 6e). Compared with other models, the d-

band center of the Fe atom in BCO<sub>2</sub> + Fe(OH)<sub>2</sub><sup>+</sup> was closer to the Fermi level, which indicated that BCO<sub>2</sub> species were more suitable to serve as the electronic porters [58]. Figs. 6f and S17c depict the adsorption energy (E<sub>ads</sub>) of Fe(OH)<sub>2</sub><sup>+</sup> attached to graphene (represents PC) and four kinds of boron-containing models. Strong binding of Fe(III) on BC<sub>3</sub> (E<sub>ads</sub> = -2.747 eV) covered active boron sites, which led to its inactivation for electron transfer. On the other hand, the relatively weaker binding affinity of Fe(III) on B-O (E<sub>ads</sub> = -1.640 eV), BC<sub>2</sub>O (E<sub>ads</sub> = -1.855 eV) and C-C=C (E<sub>ads</sub> = -1.894 eV) would impede charge exchange for Fe(II) regeneration [59]. Draw on the above discussions, the moderate adsorption energy of Fe(OH)<sub>2</sub><sup>+</sup> on BCO<sub>2</sub> (E<sub>ads</sub> = -2.353 eV) enables BCO<sub>2</sub> as the pioneer to sustainably transfer electrons to Fe(III) without poisoning, which was also in line with the fact that the proportion of adsorbed Fe species shrunken with the increase of boron content (BCO<sub>2</sub> is the main boron species, Figs. 3a and 4f). This further substantiated that BCO<sub>2</sub> is the primary active boron species in BPC.

### 3.6. Identification of active reactive species and dominant oxidation mechanism

Electron spin resonance (ESR) test, quenching experiment and probe experiment were carried out to qualitatively and quantitatively analyze the reactive species produced in BPC/Fe(III)/H<sub>2</sub>O<sub>2</sub> system, and further determine the dominant oxidation mechanism.

Figs. 7a-b and S18-S19 displayed the ESR spectra for detecting •OH, HO<sub>2</sub>/O<sub>2</sub><sup>•</sup> and <sup>1</sup>O<sub>2</sub> using DMPO and TEMP as trapping agents. BPC-30/H<sub>2</sub>O<sub>2</sub> system only detected faint signals of the DMPO-HO• and TEMP-<sup>1</sup>O<sub>2</sub> adducts, illustrating that BPC-30 alone has a limited capacity to activate H<sub>2</sub>O<sub>2</sub>. Evident DMPO-HO•, DMPO-HO<sub>2</sub>/O<sub>2</sub><sup>•</sup> and TEMP-<sup>1</sup>O<sub>2</sub> characteristic signals were all observed in the ESR spectra of Fe(III)/H<sub>2</sub>O<sub>2</sub> and BPC-30/Fe(III)/H<sub>2</sub>O<sub>2</sub> systems, indicating that these three ROS were all generated during the reaction. Notably, the DMPO-HO• and DMPO-HO<sub>2</sub>/O<sub>2</sub><sup>•</sup> signals in ESR spectra significantly increased after BPC-30 was added to Fe(III)/H<sub>2</sub>O<sub>2</sub> system, demonstrating that BPC-30

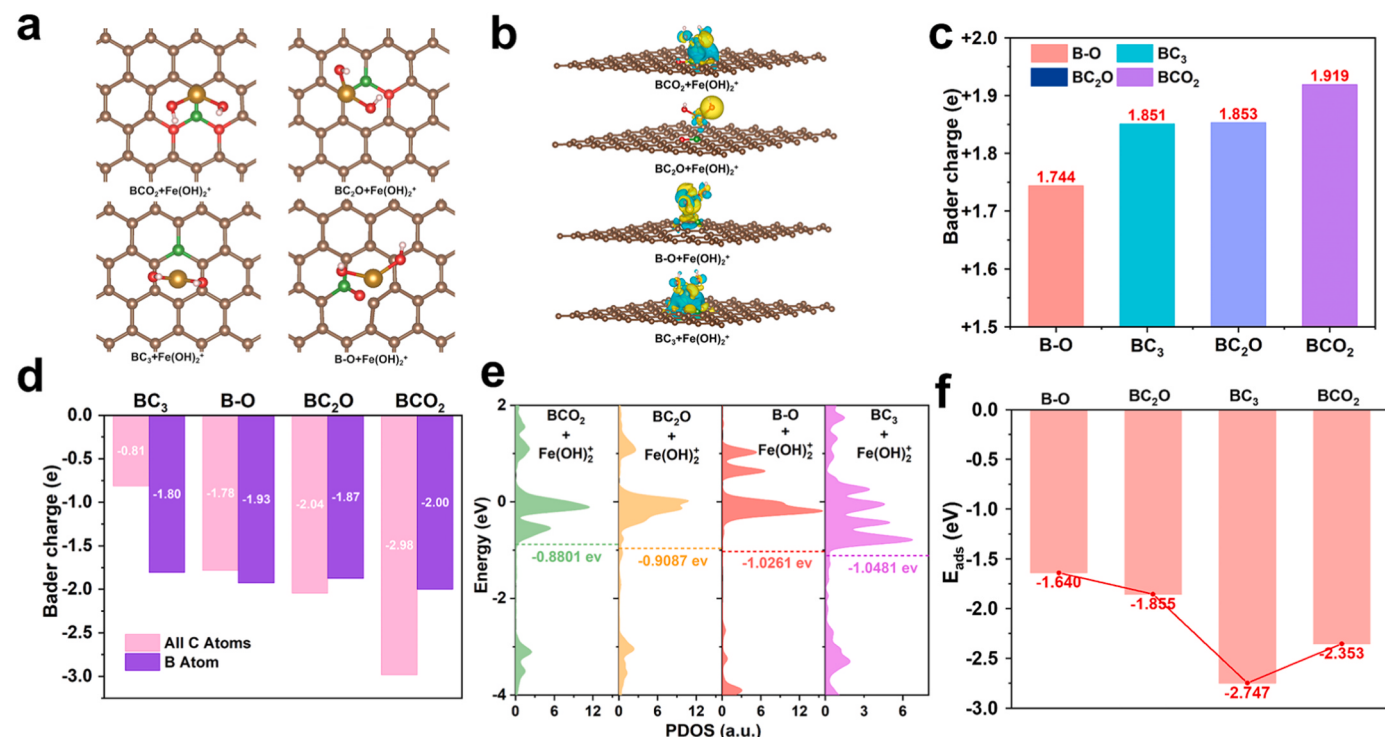


**Fig. 6.** (a) Optimized calculation models for Fe(OH)<sub>2</sub><sup>+</sup> on different boron species (top view); (b) Charge density difference diagrams for Fe(OH)<sub>2</sub><sup>+</sup> on different boron species, the electron accumulation and depletion regions are indicated by cyan and yellow, respectively (isosurface = 0.0025); (c) Bader charge of Fe atoms in Fe(OH)<sub>2</sub><sup>+</sup> on different boron species; (d) Bader charge of B and all C atoms on different configurations; (e) Comparison of PDOS of Fe atoms in different calculation models; (f) Adsorption energy values of Fe(OH)<sub>2</sub><sup>+</sup> on different boron sites.

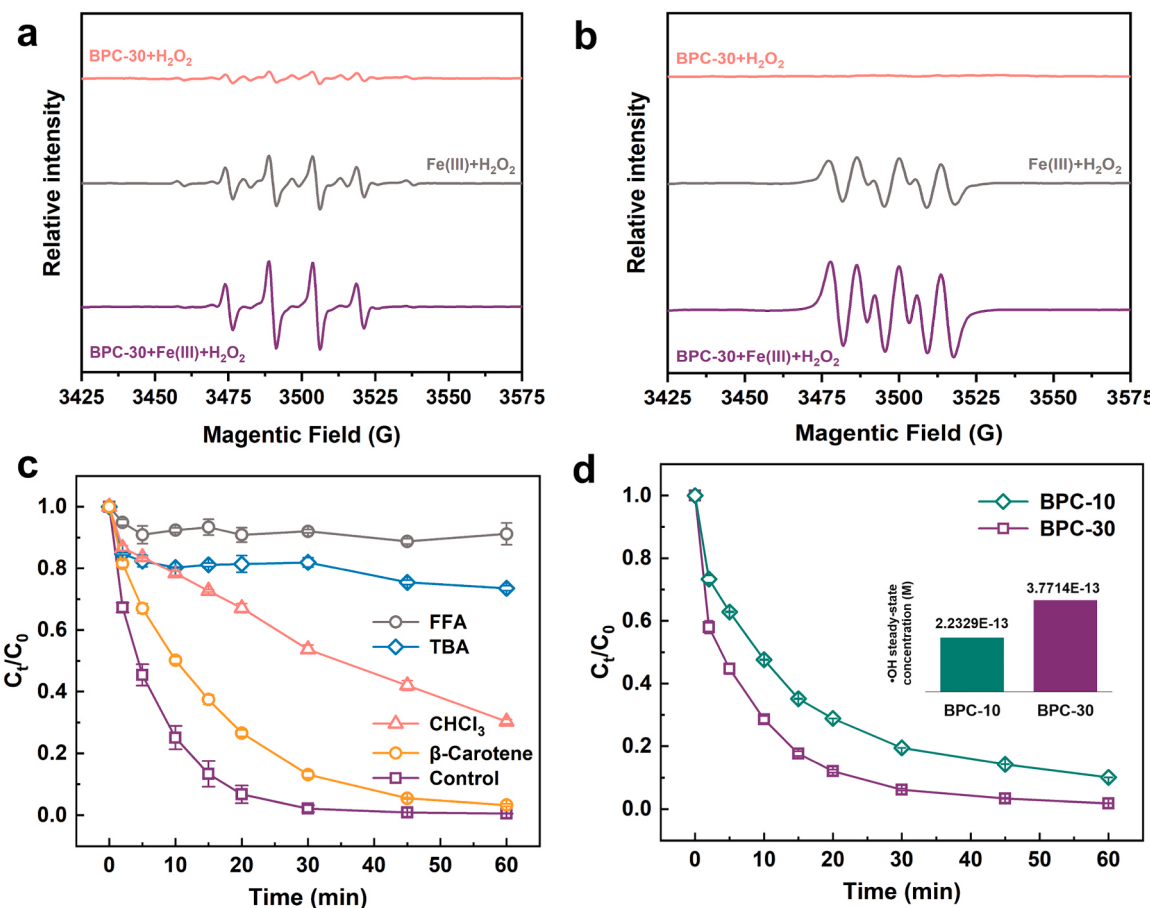


**Fig. 7.** (a) ESR spectra for detection of DMPO-HO•; (b) DMPO-HO<sub>2</sub>•/O<sub>2</sub>•; (c) Effects of various quenchants on CAF removal efficiency in BPC-30/Fe(III)/H<sub>2</sub>O<sub>2</sub> system ( $[BPC-30] = 0.04 \text{ g/L}$ ,  $[Fe(III)]_0 = 40.0 \mu\text{M}$ ,  $[H_2O_2]_0 = 2.0 \text{ mM}$ ,  $[CAF]_0 = 10.0 \text{ mg/L}$ ,  $[quencher]_0 = 20.0 \text{ mM}$ , pH 4.0, and  $T = 25^\circ\text{C}$ ); (d) Degradation of NB in BPC-10/Fe(III)/H<sub>2</sub>O<sub>2</sub> and BPC-Fe(III)/H<sub>2</sub>O<sub>2</sub> systems, inset: the calculated •OH steady-state concentrations ( $[BPC] = 0.04 \text{ g/L}$ ,  $[Fe(III)]_0 = 40.0 \mu\text{M}$ ,  $[H_2O_2]_0 = 2.0 \text{ mM}$ ,  $[NB]_0 = 10.0 \text{ mg/L}$ , pH 4.0 and  $T = 25^\circ\text{C}$ ).

promoted Fe(III) reduction by H<sub>2</sub>O<sub>2</sub> and produced more HO<sub>2</sub>•/O<sub>2</sub>• through Eq. 2, as well as, sped up the regeneration of Fe(II) and then activated H<sub>2</sub>O<sub>2</sub> to produce more •OH. In addition, the intensity of DMPO-HO• adduct in BPC-30/Fe(III)/H<sub>2</sub>O<sub>2</sub> system was evidently higher than that of PC/Fe(III)/H<sub>2</sub>O<sub>2</sub> system (Figure S19a), confirming that boron doping elevates the activity of porous carbon materials for enhancing the oxidation ability of Fe(III)/H<sub>2</sub>O<sub>2</sub> system.

To further examine the oxidation contribution of different ROS in pollutant degradation, quenching experiments were carried out. Tert-butanol (TBA,  $k_{TBA+\bullet OH} = (3.8-7.6) \times 10^8 \text{ M}^{-1}\cdot\text{s}^{-1}$ ) [12,60], chloroform (CHCl<sub>3</sub>,  $k_{CHCl_3+HO_2^\bullet/O_2^\bullet} = 3 \times 10^{10} \text{ M}^{-1}\cdot\text{s}^{-1}$ ) [61] and β-carotene ( $k_{\beta\text{-Carotene}} = (2.0-3.0) \times 10^9 \text{ M}^{-1}\cdot\text{s}^{-1}$ ) [26,62] were used as the exclusive inhibitor of •OH, HO<sub>2</sub>•/O<sub>2</sub>• and <sup>1</sup>O<sub>2</sub> respectively, while furfuryl alcohol (FFA) was used to quench <sup>1</sup>O<sub>2</sub> and •OH ( $k_{FFA+\bullet OH} = 1.2 \times 10^8 \text{ M}^{-1}\cdot\text{s}^{-1}$ ,  $k_{FFA+\bullet OH} = 1.5 \times 10^{10} \text{ M}^{-1}\cdot\text{s}^{-1}$ ) [63-66]. As shown in Fig. 7c, the addition of β-carotene only slightly slowed the degradation of CAF, and the removal rate still reached 96.72% after 60 min, indicating that the non-radical <sup>1</sup>O<sub>2</sub> oxidation contributed little to CAF elimination. After adding TBA and CHCl<sub>3</sub>, the CAF removal rate dropped to 69.68% and 26.42%, respectively. The more pronounced inhibitory effect of TBA suggested that •OH is more crucial to the degradation of CAF. The elimination rate of CAF was reduced further with the addition of FFA, and the capacity to oxidize CAF was almost completely hindered, which indicated that <sup>1</sup>O<sub>2</sub> was also engaged in the oxidation process of CAF.

Next, the presence of high-valent iron species in BPC-30/Fe(III)/H<sub>2</sub>O<sub>2</sub> system was examined. Methylphenyl sulfoxide (PMSO) can react with high-valence metal species to form the corresponding

methylphenyl sulfone (PMSO<sub>2</sub>) [67-70], which is always used as a probe compound for the detection of high-valent iron species. However, no conversion of PMSO to PMSO<sub>2</sub> was observed in BPC-30/Fe(III)/H<sub>2</sub>O<sub>2</sub> and Fe(III)/H<sub>2</sub>O<sub>2</sub> systems (Figure S20), demonstrating that the above systems did not generate high-valent iron species during the reaction. The contribution of the electron transfer pathway (ETP) was evaluated by chronopotentiometry [71-73]. As shown in Fig. 4h, after CAF was added at 2400 s, the potential did not change significantly, indicating that the ETP pathway could not cause effective oxidation of CAF [71, 74]. In conclusion, the degradation of CAF in BPC/Fe(III)/H<sub>2</sub>O<sub>2</sub> system was mostly unaffected by the non-radical oxidation pathways (<sup>1</sup>O<sub>2</sub>, high-valent iron species, and ETP); Free radical pathway is the predominant oxidation mechanism, and •OH plays a vital role in the degradation of CAF.

The •OH steady-state concentrations in different BPC/Fe(III)/H<sub>2</sub>O<sub>2</sub> systems were determined using nitrobenzene (NB) as the probe ( $k_{\bullet OH, NB} = 3.9 \times 10^9 \text{ M}^{-1}\cdot\text{s}^{-1}$ ) [75]. As shown in Fig. 7d, BPC-10 and BPC-30 co-catalytic Fe(III)/H<sub>2</sub>O<sub>2</sub> systems removed more than 90% of NB within 60 min with the  $k_{obs}$  values of  $(5.23 \pm 0.02) \times 10^{-2} \text{ min}^{-1}$  and  $(8.83 \pm 0.11) \times 10^{-2} \text{ min}^{-1}$ , respectively. As a result, the corresponding •OH steady-state concentrations were calculated to be  $(2.23 \pm 0.01) \times 10^{-13} \text{ M}$  and  $(3.77 \pm 0.05) \times 10^{-13} \text{ M}$ , respectively. It was evident that boron doping improved the effectiveness of pollutant degradation by promoting the formation of •OH in the system.

### 3.7. Application trial of BPC/Fe(III)/H<sub>2</sub>O<sub>2</sub> system in water treatment

Effectively eliminating organic micropollutants, which are omnipresent in surface waters worldwide, remains a harsh challenge in actual water treatment [76,77]. The fascinating co-catalytic performance of BPC encouraged us to further realize its device integration for micro-polluted water decontamination. Thus, a continuous flow catalytic reactor based on a water-purification membrane was constructed. Specifically, the material was loaded on a polyethersulfone (PES) membrane by simple vacuum filtration and another PES membrane was attached to its surface to prevent it from dispersing into the solution, thus forming a stable sandwich-shaped BPC membrane (Fig. 8a). The obtained membrane was then assembled with an ultrafiltration cup to form a membrane filter (Fig. 8b). Fig. 8c displayed the final continuous flow device, in which a peristaltic pump was used to inject the pollutant stock solution containing Fe(III) and H<sub>2</sub>O<sub>2</sub> while allowing for control of the water flux. A continuous degradation experiment of CAF was conducted to examine the application potential of this device. After optimizing the reaction conditions (treatment capacity: 0.3 L/h), the removal efficiency of CAF after a single flow-through treatment reached over 87% (Fig. 8d). Most crucially, the removal efficiency remained almost constant despite the continuous treatment of 20.0 L sewage, which further proved the excellent performance of the BPC co-catalytic filter and demonstrated its feasibility for long-term operation. Due to its high removal efficiency, stability and low cost, we consider it to be an ideal water purification device for treating micropollutants.

## 4. Conclusion

In this study, boron-doped porous carbon (BPC) was prepared

through a facile method for constructing a novel co-catalytic oxidation system. A small amount of BPC (0.04 g/L) significantly enhanced the oxidation performance of Fe(III)/H<sub>2</sub>O<sub>2</sub> system, which realized water decontamination via •OH-dominated radical pathway. The doping of boron not only optimized the pore structure of the material but also enhanced its electron transfer ability. Besides, boron doping improved the redox potential of Fe(III) and reduced the reaction barrier of Fe(III)/Fe(II) cycle in BPC/Fe(III)/H<sub>2</sub>O<sub>2</sub> system. Interestingly, the Fe(III) reduction pathway was found to be regulated by adjusting the amount or type of heteroatom. The increase of boron species in the material enhanced Fe(III) reduction by H<sub>2</sub>O<sub>2</sub> and direct electron supply from the cocatalyst, differing from P, N, and S species. In addition, BCO<sub>2</sub> was confirmed as the active species on BPC, and the activity origin of BCO<sub>2</sub> was further unveiled by DFT modelling. Importantly, the co-catalytic membrane developed from BPC worked well in the flow-through process for micro-polluted water purification. Our research supplies novel insights into the co-catalytic mechanism of heteroatom-doped carbon-based Fenton-like technology.

## CRediT authorship contribution statement

**Huanjing Zhang:** Investigation, Methodology, Formal analysis, Computation, Writing -original draft. **Cheng Chen:** Conceptualization, Investigation, Methodology, Formal analysis, Supervision, Writing -original draft, Writing - review & editing. **Muke Lin:** Investigation, Formal analysis. **Lingzhi Zhou:** Software, Computation. **Hailing Wen:** Investigation, Validation. **Tao Zhong:** Validation, Software. **Huinan Zhao:** Validation. **Shuanghong Tian:** Validation, Supervision. **Chun He:** Resources, Supervision, Funding Acquisition, Writing - review & editing.

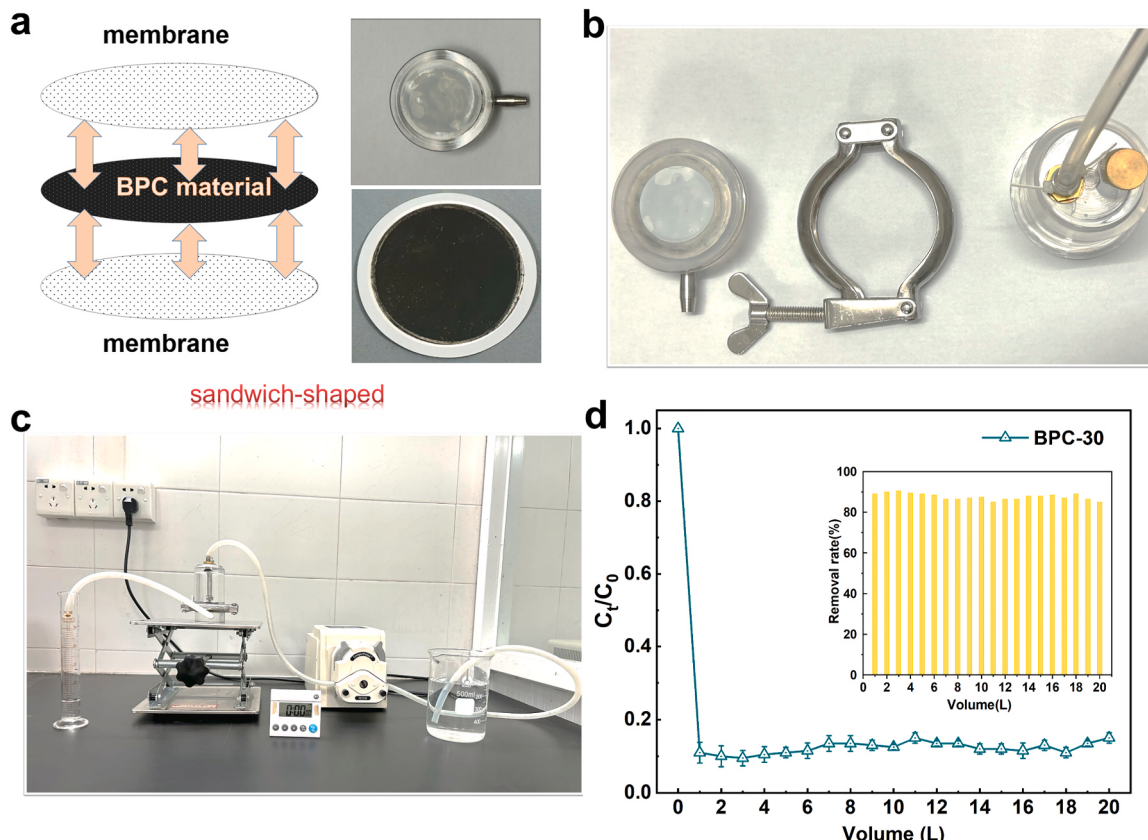


**Fig. 8.** (a) Schematic diagram and actual picture of co-catalytic filtration membrane equipped with BPC material; (b) Top view of core components of the membrane reactor; (c) Actual operation photograph of continuous degradation of CAF in the flow-through membrane reactor; (d) Continuous degradation of CAF by BPC/Fe(III)/H<sub>2</sub>O<sub>2</sub> system in a flow-through membrane reactor, inset: removal rate ([BPC] = 0.10 g/L, [Fe(III)]<sub>0</sub> = 80.0 μM, [H<sub>2</sub>O<sub>2</sub>]<sub>0</sub> = 2.0 mM, [CAF]<sub>0</sub> = 2.0 mg/L, pH 4.0 and T = 25 °C, treatment capacity: 0.3 L/h).

## Declaration of Competing Interest

The authors declare that they have no known competing financial interests or personal relationships that could have appeared to influence the work reported in this paper.

## Data Availability

Data will be made available on request.

## Acknowledgements

The authors thank the National Natural Science Foundation of China (Nos. 52070195, 21876212), Guangdong Basic and Applied Basic Research Foundation (No. 2023A1515012198) for financially supporting this work.

## Appendix A. Supporting information

Supplementary data associated with this article can be found in the online version at [doi:10.1016/j.apcatb.2023.123535](https://doi.org/10.1016/j.apcatb.2023.123535).

## References

- [1] F. Chen, W. Ma, J. He, J. Zhao, Fenton degradation of malachite green catalyzed by aromatic additives, *J. Phys. Chem. A* 106 (2002) 9485–9490.
- [2] J.J. Pignatello, D. Liu, P. Huston, Evidence for an additional oxidant in the photoassisted Fenton reaction, *Environ. Sci. Technol.* 33 (1999) 1832–1839.
- [3] Y. Qin, L. Zhang, T. An, Hydrothermal carbon-mediated Fenton-like reaction mechanism in the degradation of alachlor: direct electron transfer from hydrothermal carbon to Fe(III), *ACS Appl. Mater. Interfaces* 9 (2017) 17115–17124.
- [4] Z. Tang, R. Yin, W. Qu, H. Liu, H. Luo, D. Xia, Y. Huang, L. Shu, C. He, Flower pollen-based photosensitization process for enhanced solar disinfection of drinking water: reactor design and inactivation mechanisms, *ACS EST Eng.* 2 (2022) 629–641.
- [5] W. Qu, C. Chen, Z. Tang, D. Xia, D. Ma, Y. Huang, Q. Lian, C. He, D. Shu, B. Han, Electron-rich/poor reaction sites enable ultrafast confining Fenton-like processes in facet-engineered BiOI membranes for water purification, *Appl. Catal. B: Environ.* 304 (2022), 120970.
- [6] K. Deng, Y. Gu, T. Gao, Z. Liao, Y. Feng, S. Zhou, Q. Fang, C. Hu, L. Lyu, Carbonized MOF-coated zero-valent Cu driving an efficient dual-reaction-center Fenton-like water treatment process through utilizing pollutants and natural dissolved oxygen, *ACS EST Water* 2 (2022) 174–183.
- [7] Y.-d Chen, X. Duan, X. Zhou, R. Wang, S. Wang, N.-q Ren, S.-H. Ho, Advanced oxidation processes for water disinfection: Features, mechanisms and prospects, *Chem. Eng. J.* 409 (2021), 128207.
- [8] Q. Yan, J. Zhang, M. Xing, Cocatalytic Fenton reaction for pollutant control, *Cell Rep. Phys. Sci.* (2020), 100149.
- [9] C. Chen, Y. Wang, Y. Huang, J. Huo, W. Qu, D. Xia, C. He, V.K. Sharma, D. Shu, Overlooked self-catalytic mechanism in phenolic moiety-mediated Fenton-like system: formation of Fe(III) hydroperoxide complex and co-treatment of refractory pollutants, *Appl. Catal. B: Environ.* 321 (2023), 122062.
- [10] H. Zhou, H. Zhang, Y. He, B. Huang, C. Zhou, G. Yao, B. Lai, Critical review of reductant-enhanced peroxide activation processes: trade-off between accelerated  $\text{Fe}^{3+}/\text{Fe}^{2+}$  cycle and quenching reactions, *Appl. Catal. B: Environ.* 286 (2021), 119900.
- [11] Q. Yi, J. Ji, B. Shen, C. Dong, J. Liu, J. Zhang, M. Xing, Singlet oxygen triggered by superoxide radicals in a molybdenum cocatalytic Fenton reaction with enhanced REDOX activity in the environment, *Environ. Sci. Technol.* 53 (2019) 9725–9733.
- [12] L. Zhu, J. Ji, J. Liu, S. Mine, M. Matsuoka, J. Zhang, M. Xing, Designing 3D-MoS<sub>2</sub> sponge as excellent cocatalysts in advanced oxidation processes for pollutant control, *Angew. Chem. Int. Ed.* 59 (2020) 13968–13976.
- [13] M. Xing, W. Xu, C. Dong, Y. Bai, J. Zeng, Y. Zhou, J. Zhang, Y. Yin, Metal sulfides as excellent Co-catalysts for H<sub>2</sub>O<sub>2</sub> decomposition in advanced oxidation processes, *Chem* 4 (2018) 1359–1372.
- [14] J. Liu, C. Dong, Y. Deng, J. Ji, S. Bao, C. Chen, B. Shen, J. Zhang, M. Xing, Molybdenum sulfide Co-catalytic Fenton reaction for rapid and efficient inactivation of *Escherichia coli*, *Water Res.* 145 (2018) 312–320.
- [15] Q. Yan, C. Lian, K. Huang, L. Liang, H. Yu, P. Yin, J. Zhang, M. Xing, Constructing an acidic microenvironment by MoS<sub>2</sub> in heterogeneous fenton reaction for pollutant control, *Angew. Chem. Int. Ed.* 60 (2021) 17155–17163.
- [16] C. Dong, J. Ji, B. Shen, M. Xing, J. Zhang, Enhancement of H<sub>2</sub>O<sub>2</sub> decomposition by the Co-catalytic effect of WS<sub>2</sub> on the Fenton reaction for the synchronous reduction of Cr(VI) and remediation of phenol, *Environ. Sci. Technol.* 52 (2018) 11297–11308.
- [17] J. Ji, R.M. Aleisa, H. Duan, J. Zhang, Y. Yin, M. Xing, Metallic Active Sites on MoO<sub>2</sub>(110) Surface to Catalyze Advanced Oxidation Processes for Efficient Pollutant Removal, *iScience* 23 (2020), 100861.
- [18] Z. Yang, A. Yu, C. Shan, G. Gao, B. Pan, Enhanced Fe(III)-mediated Fenton oxidation of atrazine in the presence of functionalized multi-walled carbon nanotubes, *Water Res.* 137 (2018) 37–46.
- [19] J. Peng, J. Xue, J. Li, Z. Du, Z. Wang, S. Gao, Catalytic effect of low concentration carboxylated multi-walled carbon nanotubes on the oxidation of disinfectants with Cl-substituted structure by a Fenton-like system, *Chem. Eng. J.* 321 (2017) 325–334.
- [20] P. Zhou, W. Ren, G. Nie, X. Li, X. Duan, Y. Zhang, S. Wang, Fast and long-lasting iron(III) reduction by boron toward green and accelerated Fenton chemistry, *Angew. Chem. Int. Ed.* 59 (2020) 16517–16526.
- [21] H. Zhou, J. Peng, J. Li, J. You, L. Lai, R. Liu, Z. Ao, G. Yao, B. Lai, Metal-free black-red phosphorus as an efficient heterogeneous reductant to boost  $\text{Fe}^{3+}/\text{Fe}^{2+}$  cycle for peroxymonosulfate activation, *Water Res.* 188 (2021), 116529.
- [22] C. Zhou, P. Zhou, M. Sun, Y. Liu, H. Zhang, Z. Xiong, J. Liang, X. Duan, B. Lai, Nitrogen-doped carbon nanotubes enhanced Fenton chemistry: role of near-free iron(III) for sustainable iron(III)/iron(II) cycles, *Water Res.* 210 (2022), 117984.
- [23] C. Chen, L. Zhou, H. Zhang, Y. Yang, M. Lin, X. Xu, W. Qu, H. Zhao, D. Xia, C. He, Eco-friendly lignin-based N/C cocatalysts for ultrafast cyclic Fenton-like reactions in water purification via graphitic N-mediated interfacial electron transfer, *ACS EST Eng.* 3 (2023) 248–259.
- [24] H. Zhao, X. Ma, M. Lu, F. He, F. Lin, Y. Zhang, J. Zhang, P. Dong, C. Zhao, H. Sun, Melamine foam derived nitrogen and boron co-doped metal-free electrode for enhanced electro-Fenton degradation of metronidazole, *Chem. Eng. J.* 455 (2023), 140593.
- [25] X. Chen, L. Wang, W. Sun, Z. Yang, J. Jin, Y. Huang, G. Liu, Boron bifunctional catalysts for rapid degradation of persistent organic pollutants in a metal-free electro-Fenton process: O<sub>2</sub> and H<sub>2</sub>O<sub>2</sub> activation process, *Environ. Sci. Technol.* 57 (2023) 15693–15702.
- [26] T. Zeng, S. Jin, S. Li, J. Bao, Z. Jin, D. Wang, F. Dong, H. Zhang, S. Song, Covalent triazine frameworks with defective accumulation sites: exceptionally modulated electronic structure for solar-driven oxidative activation of peroxymonosulfate, *Environ. Sci. Technol.* 56 (2022) 9474–9485.
- [27] J. Yu, H. Feng, L. Tang, Y. Pang, G. Zeng, Y. Lu, H. Dong, J. Wang, Y. Liu, C. Feng, J. Wang, B. Peng, S. Ye, Metal-free carbon materials for persulfate-based advanced oxidation process: microstructure, property and tailoring, *Prog. Mater. Sci.* 111 (2020), 100654.
- [28] F. Sun, Z.B. Qu, J.H. Gao, H.B. Wu, F. Liu, R. Han, L.J. Wang, T. Pei, G.B. Zhao, Y. F. Lu, In situ doping boron atoms into porous carbon nanoparticles with increased oxygen graft enhances both affinity and durability toward electrolyte for greatly improved supercapacitive performance, *Adv. Funct. Mater.* 28 (2018).
- [29] P. Zhou, F. Cheng, G. Nie, Y. Yang, K. Hu, X. Duan, Y. Zhang, S. Wang, Boron carbide boosted Fenton-like oxidation: a novel Fe(III)/Fe(II) circulation, *Green. Energy Environ.* 5 (2020) 414–422.
- [30] P. Zhou, Y. Yang, W. Ren, X. Li, Y. Zhang, B. Lai, S. Wang, X. Duan, Molecular and kinetic insights to boron boosted Fenton-like activation of peroxymonosulfate for water decontamination, *Appl. Catal. B: Environ.* 319 (2022), 121916.
- [31] X. Qian, M. Ren, M. Fang, M. Kan, D. Yue, Z. Bian, H. Li, J. Jia, Y. Zhao, Hydrophilic mesoporous carbon as iron(III)/(II) electron shuttle for visible light enhanced Fenton-like degradation of organic pollutants, *Appl. Catal. B: Environ.* 231 (2018) 108–114.
- [32] P. Zhou, J. Zhang, Z. Xiong, Y. Liu, X. Huo, X. Cheng, W. Li, F. Cheng, Y. Zhang, C<sub>60</sub> Fullerol promoted Fe(III)/H<sub>2</sub>O<sub>2</sub> Fenton oxidation: role of photosensitive Fe(III)-Fullerol complex, *Appl. Catal. B: Environ.* 265 (2020), 118264.
- [33] H. Li, F. Zaviska, S. Liang, J. Li, L. He, H.Y. Yang, A high charge efficiency electrode by self-assembling sulphonated reduced graphene oxide onto carbon fibre: towards enhanced capacitive deionization, *J. Mater. Chem. A* (2) (2014).
- [34] W.J. Tian, H.Y. Zhang, H.Q. Sun, A. Suvorova, M. Saunders, M. Tade, S.B. Wang, Heteroatom (N or N-S)-doping induced layered and honeycomb microstructures of porous carbons for CO<sub>2</sub> capture and energy applications, *Adv. Funct. Mater.* 26 (2016) 8651–8661.
- [35] W.J. Tian, H.Y. Zhang, H.Q. Sun, M.O. Tade, S.B. Wang, Template-free synthesis of N-doped carbon with pillared-layered pores as bifunctional materials for supercapacitor and environmental applications, *Carbon* 118 (2017) 98–105.
- [36] N.E. Webb Jr., G.J. Sperandio, A.N. Martin, A study of the decomposition of glucose solutions, *J. Am. Pharm. Assoc. Am. Pharm. Assoc.* 47 (1958) 101–103.
- [37] H. Tamura, K. Goto, T. Yotsuyanagi, M. Nagayama, Spectrophotometric determination of iron(II) with 1,10-phenanthroline in the presence of large amounts of iron(III), *Talanta* 21 (1974) 314–318.
- [38] R.F.P. Nogueira, M.C. Oliveira, W.C. Paterlini, Simple and fast spectrophotometric determination of H<sub>2</sub>O<sub>2</sub> in photo-Fenton reactions using metavanadate, *Talanta* 66 (2005) 86–91.
- [39] C. Chen, T. Ma, Y. Shang, B. Gao, B. Jin, H. Dan, Q. Li, Q. Yue, Y. Li, Y. Wang, X. Xu, In-situ pyrolysis of Enteromorpha as carbocatalyst for catalytic removal of organic contaminants: considering the intrinsic N/Fe in Enteromorpha and non-radical reaction, *Appl. Catal. B: Environ.* 250 (2019) 382–395.
- [40] Z. Yang, C. Shan, B. Pan, J.J. Pignatello, The Fenton reaction in water assisted by picolinic acid: accelerated iron cycling and Co-generation of a selective Fe-based oxidant, *Environ. Sci. Technol.* 55 (2021) 8299–8308.
- [41] C. Chen, L.L. Zhou, Y.N. Huang, W.K. Wang, J. Xu, Boron regulates catalytic sites of biochar to enhance the formation of surface-confined complex for improved peroxydisulfate activation, *Chemosphere* 301 (2022), 134690.
- [42] D.W. Wang, F. Li, Z.G. Chen, G.Q. Lu, H.M. Cheng, Synthesis and electrochemical property of boron-doped mesoporous carbon in supercapacitor, *Chem. Mater.* 20 (2008) 7195–7200.
- [43] L.R. Radovic, M. Karra, K. Skokova, P.A. Thrower, The role of substitutional boron in carbon oxidation, *Carbon* 36 (1998) 1841–1854.

[44] A.C. Ferrari, Interpretation of Raman Spectra of Disordered and Amorphous Carbon, 2000.

[45] X. Duan, Z. Ao, L. Zhou, H. Sun, G. Wang, S. Wang, Occurrence of radical and nonradical pathways from carbocatalysts for aqueous and nonaqueous catalytic oxidation, *Appl. Catal. B: Environ.* 188 (2016) 98–105.

[46] W. Ma, N. Wang, T. Tong, L. Zhang, K.-Y.A. Lin, X. Han, Y. Du, Nitrogen, phosphorus, and sulfur tri-doped hollow carbon shells derived from ZIF-67/poly (cyclotriphosphazene-co-4, 4'-sulfonyldiphenol) as a robust catalyst of peroxyomonosulfate activation for degradation of bisphenol A, *Carbon* 137 (2018) 291–303.

[47] X.R. Wen, D.S. Zhang, T.T. Yan, J.P. Zhang, L.Y. Shi, Three-dimensional graphene-based hierarchically porous carbon composites prepared by a dual-template strategy for capacitive deionization, *J. Mater. Chem. A* 1 (2013) 12334–12344.

[48] J.E. Chen, X. Xiong, P. Xiao, H.B. Zhang, The catalytic effect of boric acid on polyacrylonitrile-based carbon fibers and the thermal conductivity of carbon/carbon composites produced from them, *Carbon* 48 (2010) 2341–2346.

[49] B.B. Chang, Y.Z. Guo, Y.C. Li, H. Yin, S.R. Zhang, B.C. Yang, X.P. Dong, Graphitized hierarchical porous carbon nanospheres: simultaneous activation/graphitization and superior supercapacitance performance, *J. Mater. Chem. A* 3 (2015) 9565–9577.

[50] Y. Li, J.W. Qi, J.S. Li, J.M. Shen, Y.X. Liu, X.Y. Sun, J.Y. Shen, W.Q. Han, L.J. Wang, Nitrogen-doped hollow mesoporous carbon spheres for efficient water desalination by capacitive deionization, *ACS Sustain. Chem. Eng.* 5 (2017) 6635–6644.

[51] C.K. Lam, T.C. Mak, A new layer type anionic host lattice constructed from urea, squarate, bicarbonate, and water molecules, *J. Struct. Chem.* 40 (1999) 714–720.

[52] Q. Li, T.C.W. Mak, Inclusion compounds of thiourea and peralkylated ammonium salts. Part II. Hydrogen-bonded host lattices built of thiourea and cyclic dimeric bicarbonate moieties, *J. Incl. Phenom. Mol. Recognit. Chem.* 20 (1994) 73–88.

[53] S. Yang, Z.-H. Liang, Y. Wen, C.-S. He, Z. Xiong, Y. Du, Y. Liu, H. Zhang, P. Zhou, Y. Mu, G. Yao, B. Lai, Gallic acid accelerates the oxidation ability of the peracetic acid/Fe(III) system for bisphenol a removal: fate of various radicals, *ACS EST Eng.* 3 (2023) 271–282.

[54] Q. Yan, J. Zhang, M. Xing, Cocatalytic Fenton reaction for pollutant control, *Cell Rep. Phys. Sci.* 1 (2020), 100149.

[55] S. Zhao, T. Yan, H. Wang, J. Zhang, L. Shi, D. Zhang, Creating 3D hierarchical carbon architectures with micro-, meso-, and macropores via a simple self-blown strategy for a flow-through deionization capacitor, *ACS Appl. Mater. Interfaces* 8 (2016) 18027–18035.

[56] Y. Liu, X. Xu, M. Wang, T. Lu, Z. Sun, L. Pan, Metal-organic framework-derived porous carbon polyhedra for highly efficient capacitive deionization, *Chem. Commun.* 51 (2015) 12020–12023.

[57] X. Zhou, M.-K. Ke, G.-X. Huang, C. Chen, W. Chen, K. Liang, Y. Qu, J. Yang, Y. Wang, F. Li, H.-Q. Yu, Y. Wu, Identification of Fenton-like active Cu sites by heteroatom modulation of electronic density, *Proc. Natl. Acad. Sci.* 119 (2022), e2119492119.

[58] C. Wang, Y. Liu, H. Ren, Q. Guan, S. Chou, W. Li, Diminishing the uncoordinated N species in Co-N-C catalysts toward highly efficient electrochemical CO<sub>2</sub> reduction, *ACS Catal.* 12 (2022) 2513–2521.

[59] X. Li, X. Huang, S. Xi, S. Miao, J. Ding, W. Cai, S. Liu, X. Yang, H. Yang, J. Gao, J. Wang, Y. Huang, T. Zhang, B. Liu, Single cobalt atoms anchored on porous N-doped graphene with dual reaction sites for efficient Fenton-like catalysis, *J. Am. Chem. Soc.* 140 (2018) 12469–12475.

[60] D. Xia, H. He, H. Liu, Y. Wang, Q. Zhang, Y. Li, A. Lu, C. He, P.K. Wong, Persulfate-mediated catalytic and photocatalytic bacterial inactivation by magnetic natural ilmenite, *Appl. Catal. B: Environ.* 238 (2018) 70–81.

[61] L. Wang, H. Xu, N. Jiang, Z. Wang, J. Jiang, T. Zhang, Trace cupric species triggered decomposition of peroxyomonosulfate and degradation of organic pollutants: Cu(III) being the primary and selective intermediate oxidant, *Environ. Sci. Technol.* 54 (2020) 4686–4694.

[62] Z. Zhou, J. Huang, G. Zeng, R. Yang, Z. Xu, Z. Zhou, S. Lyu, Insights into the removal of organic contaminants by calcium sulfite activation with Fe(III): performance, kinetics, and mechanisms, *Water Res.* 221 (2022), 118792.

[63] L. Peng, X. Duan, Y. Shang, B. Gao, X. Xu, Engineered carbon supported single iron atom sites and iron clusters from Fe-rich Enteromorpha for Fenton-like reactions via nonradical pathways, *Appl. Catal. B: Environ.* 287 (2021), 119963.

[64] J. Miao, W. Geng, P.J.J. Alvarez, M. Long, 2D N-doped porous carbon derived from polydopamine-coated graphitic carbon nitride for efficient nonradical activation of peroxyomonosulfate, *Environ. Sci. Technol.* 54 (2020) 8473–8481.

[65] D. Xia, H. Liu, B. Xu, Y. Wang, Y. Liao, Y. Huang, L. Ye, C. He, P.K. Wong, R. Qiu, Single Ag atom engineered 3D-MnO<sub>2</sub> porous hollow microspheres for rapid photothermocatalytic inactivation of E. coli under solar light, *Appl. Catal. B: Environ.* 245 (2019) 177–189.

[66] H. Sun, F. He, W. Choi, Production of reactive oxygen species by the reaction of periodate and hydroxylamine for rapid removal of organic pollutants and waterborne bacteria, *Environ. Sci. Technol.* 54 (2020) 6427–6437.

[67] B. Shao, H. Dong, B. Sun, X. Guan, Role of ferrate(IV) and ferrate(V) in activating ferrate(VI) by calcium sulfite for enhanced oxidation of organic contaminants, *Environ. Sci. Technol.* 53 (2019) 894–902.

[68] X. Zhang, M. Feng, C. Luo, N. Nesnas, C.-H. Huang, V.K. Sharma, Effect of metal ions on oxidation of micropollutants by ferrate(VI): enhancing role of Fe<sup>IV</sup> species, *Environ. Sci. Technol.* 55 (2021) 623–633.

[69] Y. Bao, C. Lian, K. Huang, H. Yu, W. Liu, J. Zhang, M. Xing, Generating high-valent iron-oxo —FeIV=O complexes in neutral microenvironments through peroxyomonosulfate activation by Zn–Fe layered double hydroxides, *Angew. Chem. Int. Ed.* 61 (2022), e202209542.

[70] K. Yin, L. Peng, D. Chen, S. Liu, Y. Zhang, B. Gao, K. Fu, Y. Shang, X. Xu, High-loading of well dispersed single-atom catalysts derived from Fe-rich marine algae for boosting Fenton-like reaction: role identification of iron center and catalytic mechanisms, *Appl. Catal. B: Environ.* 336 (2023), 122951.

[71] M. Yang, Z. Hou, X. Zhang, B. Gao, Y. Li, Y. Shang, Q. Yue, X. Duan, X. Xu, Unveiling the origins of selective oxidation in single-atom catalysis via Co–N<sub>4</sub>–C intensified radical and nonradical pathways, *Environ. Sci. Technol.* 56 (2022) 11635–11645.

[72] P. Duan, X. Xu, K. Guo, Q. Yue, B. Gao, Peroxyomonosulfate activation on a chainmail catalyst via an electron shuttle mechanism for efficient organic pollutant removal, *Appl. Catal. B: Environ.* 316 (2022), 121695.

[73] W. Ren, L. Xiong, X. Yuan, Z. Yu, H. Zhang, X. Duan, S. Wang, Activation of peroxydisulfate on carbon nanotubes: electron-transfer mechanism, *Environ. Sci. Technol.* 53 (2019) 14595–14603.

[74] K. Yin, Y. Shang, D. Chen, B. Gao, Q. Yue, X. Xu, Redox potentials of pollutants determining the dominate oxidation pathways in manganese single-atom catalyst (Mn-SAC)/peroxyomonosulfate system: selective catalytic mechanisms for versatile pollutants, *Appl. Catal. B: Environ.* 338 (2023).

[75] P. Duan, X. Liu, B. Liu, M. Akram, Y. Li, J. Pan, Q. Yue, B. Gao, X. Xu, Effect of phosphate on peroxyomonosulfate activation: accelerating generation of sulfate radical and underlying mechanism, *Appl. Catal. B: Environ.* 298 (2021), 120532.

[76] T.T. Guaraldo, R. Vakili, J. Wenk, D. Mattia, Highly efficient ZnO photocatalytic foam reactors for micropollutant degradation, *Chem. Eng. J.* 455 (2023), 140784.

[77] T.V. Wagner, F. Rempe, M. Hoek, E. Schuman, A. Langenhoff, Key constructed wetland design features for maximized micropollutant removal from treated municipal wastewater: a literature study based on 16 indicator micropollutants, *Water Res.* 244 (2023), 120534.